

Mechanistic understanding of the temperature dependence of crack growth rate in Alloy 600 and 316 stainless steel through high-resolution characterization

Zhao Shen^{a,*}, Martina Meisnar^a, Koji Arioka^b, Sergio Lozano-Perez^a

^a Department of Materials, University of Oxford, Parks Road, OX1 3PH Oxford, UK

^b Institute of Nuclear Safety Systems, Inc. (INSS), 64 Sata, Mihama-cho, Mikata-gun, Fuki, Mihama 919-1205, Japan

Corresponding author: zhao.shen@materials.ox.ac.uk

Abstract: Stress corrosion cracking of Alloy 600 (A600) and 316 stainless steel (316SS) exposed to simulated pressurized water reactor primary water at temperatures of 320-360°C has been investigated and compared. Intergranular oxidation developed ahead of all crack tips prepared from these two alloys. High-resolution characterization reveals that there are two main rate-controlling mechanisms contributing to crack propagation: a diffusion-based and a mechanical deformation-based. The different temperature dependence of crack growth rate (CGR) in A600 and 316SS can be explained after confirming that the two rate-controlling mechanisms exhibit different “weights” in the two alloys. The diffusion-based mechanism plays a dominant role in accelerating the CGR of A600, while the mechanical deformation-based mechanism is responsible for the observed CGR decrease of 316SS at higher temperatures.

Key words: Transmission electron microscopy; transmission Kikuchi diffraction; stress corrosion cracking; intergranular failure; temperature dependence.

1. Introduction

Alloy 600 (A600) is a key material used within the primary circuit of pressurized water reactors (PWRs), for components such as reactor pressure boundary nozzle assemblies and steam generator tubing [1, 2]. This material however, is known to have much high stress corrosion cracking (SCC) susceptibility in high temperature water, an issue which affects many commercial PWRs. Therefore, to extend the in-service lifetime, a greater understanding of the cracking behavior and how such cracks can be mitigated is required. After many decades of investigation, numerous factors which impact upon SCC susceptibility have been identified, including material composition [1, 3, 4], temperature [4-8], heat-treatment [9-12], water chemistry [2, 13, 14], grain boundary character [15, 16], mechanical deformation [17, 18]. Among these factors, temperature is identified to be an important one that can remarkably affect the crack growth rate (CGR) of SCC [4-8]. The different temperature dependences of CGR in austenitic alloys, as studied by

Arioka et al. [4], namely Alloy 690, Alloy 800, A600, and 316SS are the basis for this study. In a number of experiments, the existence of a peak temperature, after which the CGR decreases, was observed, although this was not the case for A600. Although the different dependences of temperature on CGR, referred to as CGR-temperature, were reported [4-8], the reasonable explanations for these observations are still under investigation.

According to previous reports in the literature [3, 19-25], grain boundaries ahead of SCC crack tips were always observed oxidized. The oxidized grain boundaries have been proved to be brittle and easily cracked under the micromechanical testing [26-28]. After more than 50 oxidized grain boundaries were micromechanically tested, Dohr et al. [26] found that none of the cracks propagated beyond the oxidized grain boundaries. As a result, the authors proposed that intergranular oxidation is a prerequisite for intergranular SCC (IGSCC) to occur and the factors that can affect oxidation then can affect crack propagation. Similar results were also reported by other researchers [3, 19, 20, 24, 25, 29-32]. In a recent study of temperature dependence of CGR of 316SS, Meisnar et al. [19] proposed that at least two mechanisms seem to operate: a “thermally-activated elemental diffusion and oxidation” mechanism and a “localized deformation” mechanism. The authors considered that the decrease of CGR at higher temperatures was the combined effect of these two rate-controlling mechanisms. The contribution from the deformation-based mechanism was originally quantified by measuring local matrix lattice rotation around the crack tip.

Following Meisnar’s work [19] that CGR of 316SS exposed to PWR primary water decreased with temperature within the range of 320-360°C, while CGR of A600 exhibited the opposite trend under the same conditions [4]. In the current study, a new approach was developed to better quantify the effects of the diffusion-based mechanism and the mechanical deformation-based mechanism on CGR. By expanding the methodology proposed by Meisnar et al. [19], the CGR-temperature behavior of A600 has been studied in detail, allowing the comparison with the CGR-temperature behavior of the 316SS. The results obtained in this study for these two materials are compared and discussed, allowing for a better understanding of the operating SCC mechanisms.

2. Materials and Methods

The crack tips examined in the current study were prepared from 20% cold-worked A600 tested at 320°C, 340°C, and 360°C under simulated PWR primary water (hydrogenated water: 500 ppm B + 2 ppm Li + 30 cc/kg dissolved H₂). The SCC tests were conducted in an autoclave at a constant load of 30 MPa m^{1/2} by the institute of nuclear safety systems (INSS) using pre-cracked 1/2T compact tension (CT) specimens, which were extracted in the T-L orientation (crack growth direction parallel to the rolling direction and crack plane perpendicular to the plane of the plate). Prior to autoclave testing and cold rolling, the specimens were mill-annealed in air at 930°C followed by water quenching. The microstructure of the material is shown in Fig. 1 and the material composition is shown in Table 1. The grain boundary character distribution map shows that the coincidence site lattice grain boundaries mainly consist of twin boundaries and the Kernel misorientation (KMO) map shows that the deformation in A600 was not

uniform (see Fig. 1). The average grain size of A600 was 120 μm . Due to the relatively high C content in A600, the heat treatment used for this material introduced carbide precipitation at the grain boundaries, resulting in intergranular Cr depletion. The intergranular carbide coverage was measured to be around 30%. After autoclave testing the surface containing the cracks was ground with SiC paper, followed by polishing with 1- μm diamond suspension. A mirror-finished surface was obtained after 20 minutes of final treatment with colloidal silica where the SCC crack tips could be easily observed.

Table 1 Chemical content of the alloy used in this study (wt.%)

Material	C	Cr	Fe	Si	Mn	P	S	Cu	Mo	Ni
A600	0.06	16.02	6.94	0.33	0.35	0.006	<0.001	0.03	-	76.26
316SS	0.046	17.28	65.89	0.43	1.81	0.012	0.001	-	2.48	12.05
A 690	0.02	32.7	8.64	0.08	0.25	0.012	0.001	-	-	57.6

To study specific crack tips, a focused ion beam (FIB) plan-view sample preparation technique was used. More details about the sample preparation with FIB can be found in [22]. Scanning transmission electron microscopy (STEM) and electron energy loss spectroscopy (EELS) were conducted with a JEOL ARM200F (cold-field emission gun) operating at 200 kV and equipped with a Quantum Gatan image filter (GIF) spectrometer. Following the analytical TEM (ATEM) analysis, transmission Kikuchi diffraction (TKD) was performed using a Zeiss Crossbeam 540 FEG-SEM equipped with an Oxford Instrument (OI) EBSD Nordlys Max 3 detector on TEM samples. The step size was set to 10 nm. After the TKD testing, the data was subsequently post-processed by the OI software Channel 5. Image quality, inverse pole figure (z-axis) (IPFZ), and misorientation (MO) maps were calculated automatically by the software. The MO maps, where each pixel represented the MO value in this pixel with regard to the average MO value of all pixels in the same grain, were used to qualitatively determine the dislocation density in the samples based on a color temperature spectrum (warmer areas such as red, orange and yellow indicated higher dislocation density than colder areas such as blue and green). It should be reminded that MO values shown in the MO line-profiles are relative (relative to the first pixel) and only the local changes (e.g. MO gradients) are important to understand local dislocation densities. The line profiles show the change of MO value on the y-axis, offering an easy way of visualizing the MO gradient. More details about the TKD analysis can be found in [19]. CGR measurements and the number of crack tips prepared from each specimen are listed in Table 2. All of the crack tips studied in this work were prepared from high angle grain boundaries (HGB).

Table 2 Data summarization for A600: test temperature; test duration; crack length; CGR; number of crack tips examined.

Specimen	Test temperature (°C)	Test duration (h)	Crack length (mm)	CGR (mm/s)	Number of crack tips
A600	320	1000	2.0	5.6×10^{-7}	3
	340	765	4.4	1.6×10^{-6}	4
	360	355	6.1	4.8×10^{-6}	2

The chemistry around the crack tips can be affected by the exposure time [19]. To minimize the influence of different exposure times, the crack tips examined in the current study were prepared from the area of deepest crack advance. These crack tips were believed to be potentially active based on the assumption that they were still propagating and likely to be exposed to PWR water for similar times before the end of autoclave testing. Since the CGRs of different materials under different temperatures were different, differences caused by the different exposure times might still exist.

It has been shown that intergranular carbides play a role on SCC propagation [10-12, 20, 24], although it is still not fully understood. As a result, to eliminate their effect, only active crack tips that did not terminate at carbides will be used, which also facilitates the comparison with 316SS, where no intergranular carbides were observed.

To better understand the effect of Cr content in different alloys on the formation of surface oxide, three austenitic alloys (A600, 316SS, and A690) coupons were autoclave tested and subsequently analyzed. The chemical composition of these three alloys can be found in Table 1. A600 and 316SS coupons were exposed to hydrogenated PWR primary water at 360°C for ~350h, while A690 was exposed to hydrogenated high temperature steam at 480°C for ~400h. After the corrosion tests, FIB was used to prepare TEM foils containing surface oxide films. More details about the sample preparation with FIB can be found in [22].

3. Results

As a continuation of our previous work [25], where the idea of precursor for crack propagation was introduced, the following sections will describe how the different precursors change with temperature.

3.1 Thermally-activated diffusion ahead of SCC crack tips

To study the effect of the diffusion-based mechanism on the CGR-temperature behavior of A600, oxidation and local chemistry around the crack tips tested at temperatures of 320-360°C were analyzed by high angle annular dark field (HAADF) imaging and EELS mapping. Crack tips are defined as the last portion of the grain boundary (oxidized or not) directly exposed to the environment. Since all the crack tips used in this study were prepared from the deepest region of SCC crack advance, they were supposed to be active at the end of the SCC testing. For the active crack tips, the region close to the crack tips was nearly free of oxide (due to short exposure time). The identification of the active crack tip positions was carried out with bright field TEM (BFTEM) imaging. The HAADF image and EELS maps Fig. 2a show the morphology and chemistry of a typical crack tip sample prepared from A600 tested at 320°C. Oxidation did not terminated at the crack tip, but further developed into the grain boundary ahead of the crack tip, forming an intergranular oxidation zone (IOZ). Fig. 2a reveals that there was a Cr-rich oxide at the crack tip and the tip of the IOZ. Ahead of the IOZ, a Cr-Fe depletion/Ni enriched zone was observed. The length of this zone was measured to be about 140 nm. The depletion of Cr and Fe ahead of the IOZ was the result of outward diffusion of metallic Cr and Fe towards the IOZ, where thermodynamically favourable oxidized species form, resulting in dealloying and the formation of a Ni-rich

region [20]. In this study, the relationship between the length of the Cr-Fe depletion zone and SCC test temperatures was used to quantify the effect of a diffusion-based mechanism on CGR-temperature behavior of A600. More details will be discussed later. Elemental distributions around the crack tips tested at 340°C and 360°C were similar to those tested at 320°C, although the IOZ was longer. The lengths of Cr-Fe depleted zone ahead of the IOZ were measured to be 320 nm (340°C) and 585 nm (360°C). Due to the pre-existent Cr-depletion in some grain boundaries, to better measure the length of diffusion-induced Cr-Fe depletion zone formed during the SCC crack propagation, the measurement was based on the length of Fe-depletion zone (see Figs. 2a and c).

3.2 Localized deformation around SCC crack tips

To investigate the effect of a mechanical deformation-based mechanism on the CGR-temperature behavior of A600, TKD was used following the method described by Meisnar et al. [19] on crack tips tested between 320-360°C. The image quality, misorientation (MO), and inverse pole figure (z-axis) (IPFZ) maps are shown in Fig 3. As shown in Fig. 3a, an intergranular precipitate was observed ahead of the crack tip, which was identified as Cr_7C_3 by TKD patterns and TEM diffraction (not shown). As shown in [19, 25], the extent of localized deformation around the crack tip was measured using two MO profiles, generating from the crack tip outwards into each of the grains. Due to the final thickness of the TEM foils used in the current study was only about 50 nm, sample bending was observed during thinning in some of the thin foils. Consequently, to accurately measure the local lattice rotation caused by the localized deformation, the lattice rotation caused by the sample bending should be subtracted. The localized region of deformation around the SCC crack tips was referred to as the LDZ. Details about how to calculate the size and lattice rotation angle of the LDZ can be found in [19, 25]. The justification for using the deformation intensity as a better way of comparing the mechanical response at the crack tip region is provided in section 1.

A typical SCC crack tip prepared from the A600 tested at 320°C was analyzed by TKD and the results are shown in Fig. 3a. The LDZ size, as shown in the MO profile 1, for the upper grain was about 105 nm. The lattice rotation in the LDZ was measured to be $1.6 \pm 1.1^\circ$. The LDZ size of the lower grain was about 180 nm, with a larger lattice rotation of $3.3 \pm 1.1^\circ$, as shown in the MO profile 2. Further observation reveals that the lattice rotation in the LDZ of the lower grain had two contributions. One was from the localized matrix deformation and the other one was from the sample bending. The part contributed by the sample bending can be calculated based on the second slope. The “corrected” lattice rotation that was only contributed by the localized matrix deformation can be determined by subtracting the lattice rotation introduced by sample bending. As shown in Fig. 3a, sample bending-induced lattice rotation in the lower grain was measured to be $0.9 \pm 1.1^\circ$. As a result, the “corrected” lattice rotation caused by the localized matrix deformation was calculated to be $2.4 \pm 1.6^\circ$. It is necessary to point out that the extent of matrix deformation around the intergranular carbides is very high (see Figs. 3a and b), but its effect on SCC crack growth is yet to be analyzed. For this reason, only crack tips not terminating at carbides were selected for this study. Localized deformation was also observed around the crack tips prepared from specimens tested at 340°C and 360°C. At 340°C, the LDZ size and lattice rotation were $1.5 \pm 0.9^\circ$ and 170 nm

in the upper grain, and $3.6 \pm 0.9^\circ$ and 260 nm in the lower grain, respectively (see Fig. 3b). For the sample tested at 360°C, the LDZ size and lattice rotation in the upper grain were 245 nm and $2.7 \pm 1.1^\circ$, and 430 nm and $4.8 \pm 1.1^\circ$ for the lower grain (see Fig. 3c).

Table 3 Average length of Cr-Fe depletion zone, LDZ size, and lattice rotation for the different samples. The parameters displayed were calculated and averaged from all crack tips from a given temperature.

Materials/Temp	Cr-Fe depletion length (nm)	LDZ size (nm)	Lattice rotation ($^\circ$)	Deformation intensity ($^\circ/\text{nm} \times 100$)
A600-320°C	121 ± 53	192 ± 83	2.3 ± 0.9	1.2 ± 0.6
A600-340°C	325 ± 67	237 ± 77	2.55 ± 1.1	1.1 ± 0.5
A600-360°C	556 ± 82	325 ± 91	3.74 ± 1.1	1.2 ± 0.4

All crack tips in Table 2 were analyzed by ATEM and TKD with the methods presented above. The length of Cr-Fe depletion zone, the LDZ size, and the lattice rotation around crack tips were determined after the analysis. To account for the statistical variations in the results obtained by ATEM and TKD, all parameters for each temperature were averaged for all samples as shown in Table 3.

3.3 Intergranular oxidation and grain boundary migration

An IOZ was observed ahead of all crack tips examined in the current study and is considered to play a significant role in the SCC crack growth [20-22, 26, 29, 30, 33]. To reveal the relationship between the intergranular oxidation and SCC propagation, high-resolution HAADF imaging and EELS analysis were conducted. The results obtained from samples tested at 320°C, 340°C, and 360°C are displayed in Figs. 4-6 and described next.

3.3.1 Crack tips tested at 320°C

Fig. 4a shows the HAADF image of the crack tip tested at 320°C. Although the crack tip region was enriched in Cr-rich oxide, the grain boundary ahead of the crack tips seemed to be not well protected because an IOZ with a length of about 130 nm was observed just ahead of the crack tip. The EELS elemental O-map (see Fig. 4b) shows that this region has been oxidized. An EELS line-scan across the IOZ is shown in Fig. 4d. It is clear that the concentrations of Cr and Ni in the IOZ were not constant and the profile of Ni is complementary to Cr. In addition, the trend of the oxygen profile across the IOZ is similar to the trend of Cr but opposite to Ni, suggesting that Cr was preferentially oxidized to form discrete Cr-rich oxide precipitates but the Ni was expelled to form metallic Ni-rich areas. This is consistent with internal oxidation and dealloying because the water chemistry used in the current study was located at the Ni-stable region (due to its high hydrogen content), where the Cr is readily oxidized while the Ni, being the most noble, is rarely oxidized, resulting in the separation of Cr-rich oxide precipitates and Ni-rich areas [2]. Similar results also were observed in A600 after internal oxidation by using atomic-resolution TEM [20] and by using 3D atom probe tomography [34].

Compared with the IOZ-metal interface, the signal intensity in the IOZ was higher, suggesting that the IOZ was more compact (high atomic density) than the IOZ-metal interface (see Fig. 4a). In addition, crack propagation was found to develop along the incoherent IOZ-metal interface but not through the IOZ. The EELS line-scan 2 reveals that Cr and Fe were enriched in this interface while Ni was depleted (see Fig. 4c). Similar phenomena were also reported by Dugdale et al. [28] and they believed that a less dense spinel oxide (richer in Fe) at the IOZ-metal interface caused preferential cracking along this interface. The formation of a Ni-rich zone ahead of the crack tips has been frequently reported in literature [3, 18, 20] and it has been proved to be the result of grain boundary migration by Burke et al. [21] through in-situ TEM. In the current study, the grain boundary migration was also observed, with a small part of upper grain growing into the lower grain. The final position of the grain boundary has been examined by electron diffraction. The original grain boundary is marked by the blue dashed line in Fig. 4a. Fig. 4b shows that the newly developed region in the upper grain (grain boundary migration zone) was depleted in Fe and Cr and enriched in Ni. The SCC crack was found to propagate along the migrated grain boundary, and the crack was full of Cr-rich oxide. Similar phenomenon was also reported by Kuang et al. [3] recently in the study of SCC in Alloy 690. To quantify the local elemental distribution, an EELS line-scan was conducted across the grain boundary migration region (Line 1 in Fig. 4a), as shown in Fig. 4c. According to the atomic ratio presented in Fig. 4c, the Ni-rich region was nearly composed of pure Ni while the Cr-rich region mainly consisted of a Cr-Fe-Ni spinel oxide. The deviations in atomic ratio might originate from the EELS measurement errors and sample thickness effects.

3.3.2 Crack tips tested at 340°C

Fig. 5 shows the crack tip prepared from the A600 tested at 340°C. Similarly to the A600 tested at 320°C, an IOZ with the length of about 250 nm was observed ahead of the crack tip and the crack propagated along one of the IOZ-metal interfaces (see Fig. 5a). The EELS line-scan across the IOZ revealed the existence of Ni-rich particles and Cr-rich oxide precipitates in the IOZ, as shown in Fig. 5d. Grain boundary migration was observed in the crack tip sample tested at 340°C and the crack propagated into the newly formed grain boundary (see Fig. 5a). Grain boundary migration was also observed in the IOZ, indicating that the grain boundary migration occurred before crack propagation. The extent of grain boundary migration at 340°C seems greater than at 320°C, as shown in Fig. 5b. To quantify the composition across this crack tip region, an EELS line-scan was conducted. Fig. 5c shows that this region mainly consisted of Cr-rich oxide, with depletion of both Ni and Fe. According to the atomic ratio acquired from the EELS line-scanning and the work conducted in literature [20, 29-32, 34], the Cr-rich oxide is likely to be a Cr-Fe-Ni spinel. The signal intensity at the IOZ-metal interface was also lower than in the IOZ. An EELS line-scan cross the IOZ shows that the interface region was enriched in Cr, Fe, and O, while depleted in Ni, which was similar to those observed in the crack tip samples tested at 320°C (see Fig. 5a).

3.3.3 Crack tips tested at 360°C

HAADF imaging, EELS mapping, and line-scans at higher resolution were also conducted on the crack tips tested at 360°C, as shown in Fig. 6a-d. An IOZ with the length

of about 380 nm was observed ahead of the crack tip (see Fig. 6a). EELS mapping shows that the IOZ suffered different extent of oxidation since the concentration of oxygen in this region was not uniform (see Fig. 6b). The chemical composition in the IOZ was similar to the crack tip samples tested at 320°C and 340°C. Grain boundary migration also occurred in the IOZ, and the extent of grain boundary migration was much greater than at 320°C and 340°C. Oxidation in the IOZ mainly occurred along the migration-induced grain boundary. An EELS line-scan (see Fig. 6d) across the IOZ shows that the migration region in the upper grain was nearly pure Ni, and was depleted in Cr and Fe. The O content in the IOZ was much higher than at 320°C and 340°C. The crack tip region was full of Cr-rich oxide, but the grain boundary oxidation was not effectively prevented. The EELS line-scan (see Fig. 6c) reveals that the oxide around the crack tip was also a Cr-Fe-Ni spinel. No preferential oxidation was observed at the IOZ-metal interface, and crack growth was observed through the IOZ and not along the IOZ-metal interface.

3.4 Oxide nanoporosity

To characterize the porosity of intergranular oxides, Fresnel contrast TEM imaging was used with a defocus value of ± 800 nm. More details of Fresnel contrast imaging are in [25]. The porous structures are nearly invisible in the focused image (see Fig. 7a), whilst the nano-pores and nano-channels are visible in the underfocused (see Fig. 7b) and the overfocused images (see Fig. 7c). In the current study, the TEM images were purposely taken at an underfocused condition, with the porous structure highlighting in white. Fig. 7b shows that a large number of pores existed in the IOZ of crack tip sample tested at 320°C. The Cr-rich oxide around the crack tip was much more porous than the other regions. Further analysis reveals that pores preferentially distributed along the IOZ-metal interface.

Fresnel contrast TEM imaging was also conducted on the crack tip samples tested at 340°C and 360°C and the corresponding results are shown in Fig. 8a and 8b, respectively. The crack tip region was also found to be more porous than the IOZ in these two samples (see Fig. 5b and 6b). The preferential distribution of pores along the IOZ-metal interface was also observed in the crack tip sample tested at 340°C (see Fig. 8a). However, pores were nearly uniformly distributed in the IOZ of the crack tip sample tested at 360°C and there was no preferential distribution of pores along the IOZ-metal interface.

3.5 Microstructure of surface oxide films

The HAADF images of the surface oxide films formed on A600, 316SS, and A690 are shown in Fig. 9a, b, and c, respectively. HAADF image is very sensitive to the atomic density of the materials and can be used to reveal porosity/voids. The inner oxide on A600 and 316SS appeared to be very porous while the inner oxide on A690 appeared to be much more compact. It is necessary to point out that A690 was exposed to hydrogenated high temperature steam at 480°C, which was different from A600 and 316SS. However, high temperature hydrogenated steam has been widely used to simulate the PWR primary water in the literature [30, 34]. As a result, the surface oxide films formed in these two different environments were believed to be still comparable, although the results were considered qualitative at this stage.

4. Discussion

Many austenitic alloys were reported to suffer SCC after exposure to the PWR primary water. To obtain the mechanistic understanding of the SCC behaviors, the factors affecting primary water SCC had been extensively studied [3, 4, 17-20], while the controlling mechanisms are still unresolved. Several models had been proposed to explain the SCC behaviors, and among them, the film rupture model, hydrogen embrittlement model, and internal oxidation model were mostly studied [23, 35-38]. Recently, the internal oxidation model, which was firstly promoted by Scott et al. [23] and further developed by following researchers [26, 27, 39], is starting to attract more attention. The basic assumption in this model is that grain boundaries are preferentially oxidized once exposed to PWR primary water, which causes grain boundary embrittlement causing them to fracture preferentially. Dugdale et al. [28] and Fujii et al. [27] proved these intergranular oxides to be brittle experimentally, by directly measuring the stress required to fracture them. Since oxidation was believed to be a thermally activated diffusion-based process, higher elemental diffusion rates at higher temperatures can lead to higher oxidation rates, which then could result in higher SCC propagation rate [40]. The mechanical deformation-based mechanism is used to describe the fact that the material can be locally softer or harder, affecting the load required to achieve the critical stress required to fracture the oxidized grain boundary. Having said that, the two mechanisms are interconnected (to some extent), since the defects in the LDZ could work as short-circuits and can also enhance oxidation [17-19, 41, 42]. The effects of these two mechanisms on CGR and the implications of the key observations reported in the previous section are discussed below.

4.1 Effect of intergranular oxidation on grain boundary failure

According to the results reported in this paper and elsewhere [19, 20, 23, 25, 29, 43], intergranular oxidation may play a significant role in the SCC propagation. The existence of an IOZ ahead of the crack tips suggests that intergranular oxidation occurred before crack propagation, which is consistent to the internal oxidation model [23]. Although the oxide formed around the crack tips was enriched in Cr, which was reported to be critical in protecting the metal from further oxidation [4, 23, 43, 44], the Fresnel contrast TEM imaging revealed that the Cr-rich oxide contained multiple voids and it is assumed to be porous, with gaps wide enough (>1 nm) to allow for water ingress. In any case, the protectiveness of the porous Cr-rich oxide was not good enough to prevent the development of oxidation into a deeper region, which oxidized the grain boundary ahead of the crack tip, resulting in the formation of IOZ.

From the results in this study and previous work [20, 29, 30, 33, 43, 44], two possible explanations for the origin of the voids/pores are proposed. The first one acknowledges that the selective oxidation of Cr and Fe will introduce vacancies at the interfaces of these phases. These vacancies can coalesce and contribute to grain boundary porosity. Selective oxidation is a well-known phenomenon affecting austenitic alloys under reductive high-temperature water conditions and has been also observed via atom probe tomography [34] and atomic-resolution TEM [20, 24]. In a most recent publication, Bruemmer et al. [32] conducted a systematic study of the intergranular oxidation in Ni-5at%X binary alloys. The results experimentally proved that once the selective oxidation occurred, such as in Ni-Cr and Ni-Al alloys, the grain boundary oxidation will be enhanced significantly.

However, there was almost no intergranular oxidation in Ni-Cu alloy, in which the selective oxidation was not able to occur since the Cu was nobler than the Ni in the water chemistry used in this work. In addition, the authors also observed cavities in the oxidized grain boundaries through TEM.

The second explanation is related to the fact that a minimum amount of Cr is needed to form protective oxide (first Cr_2O_3 and then Cr-rich spinel), which can explain why Alloy 690 has much higher SCC resistance than A600 [45, 46]. When the number of available trivalent cations (mostly Cr^{3+}) is insufficient, a defective Cr-rich spinel forms, with a high density of voids [47, 48]. To confirm this hypothesis, structures of surface oxide formed on alloys within different Cr content have been compared as part of our study. As shown in Fig. 9, the surface oxides formed on A600 and 316SS were more porous than that on Alloy 690. The inner surface oxide formed on Alloy 690 had ~38.3% at. Cr while A600 and 316SS had ~22.5 % at. and ~21.6% at., respectively. Since Cr_2O_3 requires 40 % at. (~68 % wt.), and $\text{FeCr}_2\text{O}_4/\text{NiCr}_2\text{O}_4$ require ~29 % at. (~47 % wt.), neither A600 nor 316SS can supply enough Cr to form a protective oxide. This could be responsible for the formation of a visibly defective (porous) oxide in A600 and 316SS (Fig 9a and 9b), while a much more uniform oxide formed in A690 (Fig 9c). It is interesting to note that intergranular oxides ahead of crack tips on both A600 and 316SS appear full of voids and possibly pores, since the Cr content in this part of grain boundary (Cr-Fe depleted zone) is even lower than the matrix (see Figs. 2, 4-6).

Intergranular oxides are brittle by nature and can be broken under dynamic strain, which has been experimentally proved by micromechanical testing [26-28, 49]. The existence of vacancies and pores can make it weaker. As a result, once the porous IOZ ahead of the crack tip is broken by the applied stress during SCC testing, the crack will advance and grain boundary oxidation will be further enhanced.

Although selective oxidation in the IOZ can lead to the formation of vacancies and pores, the porous structure in the IOZ of the crack tip samples tested at 320°C and 340°C was not uniform (see Fig. 7 and Fig. 8a). The density of pores was higher in the IOZ-metal interface (see Fig. 7 and Fig. 8a). The HAADF image shows that the IOZ-metal interface had lower signal intensity than the IOZ and EELS line-scanning shows that the interface contained higher content of oxygen, suggesting that IOZ-metal interface was preferentially oxidized. A similar result was also reported by Dugdale et al. [28]. The preferential oxidation and accumulation of vacancies at the IOZ-metal interface might explain why the crack preferentially propagate along the weaker IOZ-metal interface region but not through the IOZ. The underlying contributions to preferential weakening at the IOZ-metal interface might be due to the existence of higher content of vacancies at the incoherent IOZ-metal interface, enabling preferential penetration of water along the IOZ-metal interface. In contrast, oxidation is faster at 360°C. The higher defect density in the IOZ-metal interface does not appear to have the same impact between the extent of oxidation at the IOZ-metal interface and in the IOZ at this temperature. This might explain why there was no preferential cracking along the IOZ-metal interface at this temperature.

According to the results obtained in this work, the internal oxidation model would offer a plausible explanation. However, this model has been criticized due to

discrepancies between the experimentally measured grain boundary oxidation rates and the observed SCC CGR (up to 100x) [50, 51]. This discrepancy might come from the method used in measuring the grain boundary oxidation rate. In the literature [30, 43], oxidation rates are measured after exposing coupons to high temperature water or air, and measurements are averaged over the whole exposed surface. However, grain boundaries oxidize preferentially on these alloys and have faster oxidation rates. More importantly, since stress plays a significant role in SCC [17, 19], it is necessary to take it properly into account. The enhanced grain boundary oxidation under stress has been proved by Lozano-Perez et al. [17] through comparing the intergranular oxidation depth in a stress-free 304SS and a stressed 304SS. Even though the stress increased the intergranular oxidation by up to 100x in this study, the applied stress is distributed evenly on the specimen. At a crack tip, a higher stress concentration is expected which is likely to produce even faster oxidation rates.

4.2 Potential role of grain boundary migration in SCC

Recently, grain boundary migration in Ni-based alloys has started to be frequently reported after exposure to a hydrogenated high temperature aqueous environment [3, 30, 39]. The authors believed that the observed grain boundary migration was the result of diffusion of solute elements. As a result, it was termed as diffusion-induced grain boundary migration (DIGM). DIGM was observed along the SCC crack and at the grain boundary ahead, indicating it occurred before SCC growth. Although a similar phenomenon was observed by Langelier et al. [39] and Bertali et al. [30] when A600 was exposed to 480°C hydrogenated steam environment, the environment in this study was PWR primary water and the test temperature was lower. Consequently, the observed DIGM might be enhanced by some other factors such as the applied stress during the SCC testing [52]. The extent of DIGM (estimated by the width of the affected zone) was observed to be enhanced by temperature, suggesting that DIGM is a thermally activated process [30, 34, 39].

In reference [39], the authors observed grain boundary migration in solution-annealed and thermally-treated A600. Due to the existence of intergranular carbides in the thermally-treated A600, the grain boundary migration was significantly suppressed. However, higher extent of grain boundary migration in solution-annealed A600 led to deeper grain boundary oxidation than in thermally-treated A600. Thus, the authors suggested that grain boundary migration could accelerate intergranular oxidation. Since the intergranular oxidation rate is connected with the SCC crack growth rate [20, 30, 33] and grain boundary migration was also found in the samples used in this study (see Fig. 4-6), grain boundary migration is believed to play a role in SCC.

Grain boundary migration is characterized by Fe/Cr-depleted and Ni-rich regions. According to the results discussed in the section 4.1, the depletion of Cr can not only enhance grain boundary oxidation but also result in the formation of porous Cr-rich oxide due to the insufficient supply of Cr, which will increase SCC propagation. However, since the extent of grain boundary migration that occurred in this study was much lower than in [39], and grain boundary migration is also a thermally-activated process (see section 3.3), its potential role in SCC can be considered an integral part of the diffusion-based mechanism.

The potential relationship between the localized deformation around crack tips and the migration direction of DIGM has been examined in this work. However, no correlation was observed. This could mean that localized deformation around crack tips might not be the dominant factor for DIGM, or that it can only be explained when a 3D analysis rather than 2D (as in a TEM sample) is performed.

4.3 Quantification of the role of diffusion-based mechanism on CGR

A higher elemental diffusion rate could lead to a higher oxidation rate and in turn to a higher CGR [19, 40]. For this reason, the length of the Cr-Fe depleted zone ahead of the crack tips was used to quantify the “weight” of the diffusion-based mechanism on CGR. There are two reasons to focus on this parameter. Firstly, the Cr-Fe depleted zone was observed ahead all of the crack tips studied in this work. Secondly, the length of this zone increased with rising temperature, indicating that diffusion of Cr and Fe is a thermally-activated process.

It is necessary to point out that the length of Cr-Fe depleted zone is not only affected by the elemental diffusion rate but also affected by exposure time. Since all of the crack tips used in this study were prepared from the deepest region of SCC advance, the exposure time for them was assumed to be similar.

4.4 Quantification of the role of mechanical deformation-based mechanism on CGR

A measurement of the dislocation density in the LDZ could be used to quantify the role of the mechanical deformation-based mechanism on CGR. In this work, we introduce the concept of deformation intensity, a more appropriate parameter to define the mechanical response at the crack tip. According to the work conducted by Ashby [53], the matrix lattice rotation gradients can be related linearly to dislocation densities (deformation intensity). The lattice rotation gradient can be calculated according to the lattice rotation and localized deformation zone (LDZ) size as Lattice rotation gradient = Lattice rotation/LDZ size. The dislocation density can be quantify through conducting high-resolution TKD, as shown in [25], followed by geometrically necessary dislocation (GND) analysis, but it is very time consuming. Our preliminary comparisons show that deformation intensity compares well, at least qualitatively, to GND densities. Measuring the dislocation density around the crack tip can effectively reveal how “soft” or “hard” the material is in that region, controlled by how easily dislocations emitted from the crack tip can move away. If a high-density of dislocations is found, the material will be locally harder and a lower critical stress will be needed to fracture the oxidized grain boundary ahead of the crack tip and vice-versa. Therefore, we refer to the localized matrix lattice rotation gradient as deformation intensity, and use it to estimate the linear dislocation density in the LDZ qualitatively. More details can be found in [25, 53].

The applied stress during SCC testing introduces localized deformation around the crack tip [19, 25, 54, 55], in the form of increased dislocation densities. This can be a measure of how easily the new dislocations emanating from the crack tip can move away, with the material being “softer” for lower dislocation densities or “harder” for higher. In addition, high dislocation densities could accelerate diffusion of metallic and non-metallic elements, resulting in faster oxidation in this zone.

4.5 Differences in temperature dependence of CGR in A600 and 316SS

In the study of CGR-temperature behavior of 316SS, Meisnar et al. [19] explained the decline of CGR of 316SS at temperatures of 320-360°C as the combined effect of a diffusion-based mechanism and a mechanical deformation-based mechanism. As shown in Fig. 11b, the plot deformation intensity vs. temperature correlates well with the curve of CGR vs. temperature. Equally, the lattice rotation in the LDZ (not plotted) also decreases with temperature (7.6°, 5.8° and 2.6° for the temperatures studied, as shown in [19], Fig. 10), while the size of the LDZ remains more or less constant. The “weight” of a diffusion-based mechanism was not properly quantified in [19]. As a result, in the current study the length of the Cr-Fe depletion zone was measured on all the samples from that study, as shown in Fig. 11a. This length exhibits little change with temperature, indicating that the role of a diffusion-based mechanism on CGR-temperature behavior of 316SS is almost negligible in the temperature range 320-360°C. The two curves plotted in Fig. 11b show similar progression, suggesting that localized deformation around crack tips played a dominant role in restraining CGR of 316SS at temperatures of 320-360°C.

Similar plots for A600 are shown in Figs. 11c and 11d. The CGR versus test temperature curve is also included in these two figures for comparison. Fig. 11d shows that the deformation intensity was nearly independent of the SCC test temperature. The lattice rotation in the LDZ (not plotted) increased slightly with temperature (2.3°, 2.5° and 3.7° for the temperatures studied, as shown in Table 3), with the size of the LDZ also remaining more or less constant. Both parameters only change slightly with temperature, suggesting that the mechanical deformation-based mechanism does not play a dominant role in accelerating crack propagation with increasing temperature in A600. Fig. 11c shows that the length of the Cr-Fe depletion zone increased monotonously at temperatures of 320-360°C, which correlated well with the CGR versus temperature curve, implying that the diffusion-based mechanism plays a more important role in accelerating the CGR of A600.

The situation in 316SS is significantly different to A600 in that the CGR decreased above a certain temperature [19]. ATEM analysis [19] revealed that the length of Cr-Fe depleted zone formed ahead of the IOZ of 316SS was much shorter than that observed in A600 and the length of this zone was nearly independent to the SCC test temperature (see Fig. 11a). However, TKD analysis [19] revealed that the deformation intensity around the crack tips of 316SS was more sensitive to the SCC test temperature, decreasing remarkably after a peak temperature (320°C). This might suggest that a lower number of dislocations accumulate around the crack tip region (since they are able to move away) with increasing temperature. However, line profiles in 316SS were acquired along regions in between deformation bands, to avoid the discontinuity at their interfaces. This is an acceptable approach if the deformation band density is low and does not dominate the grain boundary length. Once deformation bands originate, plastic deformation is mostly restricted to slip inside deformation bands, as shown by Gioacchino et al. [56]. That form of localized deformation is missing from this analysis and could explain the higher local softening experience at higher temperatures by 316SS. In other words, in 316SS, as the temperature increases, fewer dislocations accumulate in the crack tip region in between deformation bands, making the material locally softer and making it harder for the critical stress required to fracture the oxidized grain boundary to be reached.

It is necessary to point out that although the contents of dissolved hydrogen at different temperatures were set to be the same (30 cc/kg), the temperature was reported to affect the position of the Ni/NiO phase boundary [2, 57]. As a result, the actual electrochemical potentials at different temperatures were different, which could affect the SCC CGR of both alloys. Considering the observed significant differences (chemically and mechanically) around the crack tips, the effect of electrochemical potential might not be the dominant factor for the different temperature dependences studied in this work. A more detailed study of the oxide composition would be ideal to shed light on this possibility, e.g. atom probe tomography (APT) characterization, and will be considered for future works.

5. Conclusions

It is proposed that intergranular oxidation ahead of crack tips in A600 plays an important role in SCC propagation, making it a necessary precursor for crack propagation. The insufficient Cr content, the selective oxidation of Cr and Fe, and the applied stress lead to the formation of porous and brittle intergranular oxide in A600, which does not efficiently protect the metal from further oxidation. The porous and brittle intergranular oxide can be preferentially broken by applied stress, resulting in crack propagation and further oxidation. The selective oxidation of Cr and Fe during crack propagation lead to the formation of a Cr-Fe depleted zone ahead of crack tip, which further enhances the formation of a porous and brittle oxidized grain boundary.

The different CGR-temperature behavior of A600 and 316SS exposed to simulated PWR primary water at temperatures of 320-360°C has been investigated and compared. Two rate-controlling factors are proposed to explain the CGR-temperature behavior: a diffusion-based mechanism and a mechanical deformation-based mechanism. The effects of these two rate-controlling mechanisms on the CGR-temperature behavior have been quantified and discussed. We propose that both mechanisms are responsible for the observed CGR-temperature behavior but have significantly different weights across the range of temperatures studied for each alloy.

Acknowledgements

The authors would like to thank INSS (Japan) for providing the samples used in this study and for useful discussions. Zhao Shen is grateful to China Scholarship Council for providing financial support. The EPSRC (EP/K040375/1, EP/N010868/1 and EP/R009392/1) grants are also acknowledged for funding this research. Profs Peter Andresen and Angus Wilkinson are also acknowledged for useful discussions.

References

[1] H. Coriou, L. Crall, Y. L. Gall, S. Vettier, 3rd Metallurgy Conf. on Corrosion, Saclay (Amsterdam, The Netherlands: North Holland Publishing Co., 1959), 1960, pp. 161-169.

- [2] P.L. Andresen, J. Hickling, A. Ahluwalia, J. Wilson. Effects of hydrogen on stress corrosion crack growth rate of nickel alloys in high-temperature water. *Corrosion*, 64(2008): 707-720.
- [3] W. Kuang, M. Song, G.S. Was. Insights into the stress corrosion cracking of solution annealed alloy 690 in simulated pressurized water reactor primary water under dynamic straining, *Acta Materialia*, 151(2018): 321-333.
- [4] K. Arioka, T. Yamada, T. Miyamoto, M. Aoki. Intergranular Stress Corrosion Cracking Growth Behavior of Ni-Cr-Fe Alloys in Pressurized Water Reactor Primary Water. *Corrosion*, 70(2014): 695-707.
- [5] T. Moss, G.S. Was. Accelerated stress corrosion crack initiation of alloys 600 and 690 in hydrogenated supercritical water. *Metallurgical and Materials Transactions A*, 48(2017): 1613-1628.
- [6] P. L. Andresen. Effects of temperature on crack growth rate in sensitized type 304 stainless steel and alloy 600. *Corrosion* 49(1993): 714-725.
- [7] S. M. Bruemmer, M. J. Olszta, D. K. Schreiber, N. R. Overman, M. B. Toloczko. Characterizations and Stress Corrosion Cracking Evaluations of Alloy 600 CRDM Nozzle Heats from the Davis Besse Nuclear Power Plant. NRC Report, August (2013).
- [8] R.B. Rebak, Z. Szklarska-Smialowska. The mechanism of stress corrosion cracking of alloy 600 in high temperature water. *Corrosion Science*, 38(1996): 971-988.
- [9] C. García, F. Martín, P. De Tiedra, J.A. Heredero, M.L. Aparicio. Effects of prior cold work and sensitization heat treatment on chloride stress corrosion cracking in type 304 stainless steels. *Corrosion science*, 43(2001): 1519-1539.
- [10] K. Arioka, T. Yamada, T. Terachi, G. Chiba. Influence of carbide precipitation and rolling direction on intergranular stress corrosion cracking of austenitic stainless steels in hydrogenated high-temperature water. *Corrosion*, 62(2006): 568-575.
- [11] S. M. Bruemmer, M. J. Olszta, M. B. Toloczko, L. E. Thomas. Proceedings of the 15th International Conference on Environmental Degradation of Materials in Nuclear Power Systems—Water Reactors, Springer, Cham, 2011, pp. 301-314.
- [12] M. B. Toloczko, M. J. Olszta, S. M. Bruemmer. Proceedings of the 15th International Conference on Environmental Degradation of Materials in Nuclear Power Systems—Water Reactors, Springer, Cham, 2011, pp. 91-107.
- [13] Z. Szklarska-Smialowska, Z. Xia, R. R. Valbuena. Mechanism of crack growth in alloy 600 in high-temperature deaerated water. *Corrosion*, 56(1994):676–681.
- [14] R. J. Jacko, R. E. Gold. Crack growth rates in primary side materials in elevated pH PWR water. In 12th international conference on environmental degradation of materials in nuclear power systems – water reactors, Salt Lake City, Utah, August 2005. TMS (The Minerals, Metals & Materials Society).
- [15] B. Alexandreanu, B. H. Sencer, V. Thaveeprungsriporn, G. S. Was. The effect of grain boundary character distribution on the high temperature deformation behavior of Ni–16Cr–9Fe alloys, *Acta Materialia*, 51(2003): 3831–3848.
- [16] Z. Lu, T. Shoji, F. Meng, H. Xue, Y. Qiu, Y. Takeda, K. Negishi. Characterization of microstructure and local deformation in 316NG weld heat-affected zone and stress corrosion cracking in high temperature water, *Corrosion Science*, 53(2011):1916-1932.

- [17] S. Lozano-Perez, K. Kruska, I. Iyengar, T. Terachi, T. Yamada. The role of cold work and applied stress on surface oxidation of 304 stainless steel. *Corrosion Science*, 56(2012): 78-85.
- [18] T. Terachi, T. Yamada, T. Miyamoto, K. Arioka. SCC growth behaviors of austenitic stainless steels in simulated PWR primary water. *Journal of Nuclear Materials*, 426(2012): 59-70.
- [19] M. Meisnar, A. Vilalta-Clemente, M. Moody, K. Arioka, S. Lozano-Perez. A mechanistic study of the temperature dependence of the stress corrosion crack growth rate in SUS316 stainless steels exposed to PWR primary water. *Acta Materialia*, 114 (2016): 15-24.
- [20] M. Sennour, P. Laghoutaris, C. Guerre, R. Molins. Advanced TEM characterization of stress corrosion cracking of Alloy 600 in pressurized water reactor primary water environment. *Journal of Nuclear Materials*, 393(2009): 254-266.
- [21] M. G. Burke, G. Bertali, E. Prestat, F. Scenini, S. J. Haigh. The application of in situ analytical transmission electron microscopy to the study of preferential intergranular oxidation in alloy 600. *Ultramicroscopy*, 176(2017): 46-51.
- [22] S. Lozano-Perez. A guide on FIB preparation of samples containing stress corrosion crack tips for TEM and atom-probe analysis. *Micron*, 39(2008): 320-328.
- [23] P.M. Scott, M. Le Calver, "Some possible mechanisms of intergranular stress corrosion cracking of alloy 600 in PWR primary water", In *Proceedings of the sixth international symposium on environmental degradation of materials in nuclear power systems-water reactors*, (TMS, 1993), 657-665.
- [24] Y. S. Lim, S. W. Kim, S. S. Hwang, H. P. Kim, C. Jang. Intergranular oxidation of Ni-based Alloy 600 in a simulated PWR primary water environment. *Corrosion Science*, 108(2016): 125-133.
- [25] Z. Shen, K. Arioka, S. Lozano-Perez, A mechanistic study of SCC in Alloy 600 through high-resolution characterization, *Corrosion Science*, 132(2018): 244-259.
- [26] J. Dohr, D.E. Armstrong, E. Tarleton, T. Couvant, S. Lozano-Perez. The influence of surface oxides on the mechanical response of oxidized grain boundaries. *Thin Solid Films*, 632(2017):17-22.
- [27] K. Fujii, T. Miura, H. Nishioka, K. Fukuya. Degradation of grain boundary strength by oxidation in alloy 600. *Materials transactions*, 52(2011): 1447-1458.
- [28] H. Dugdale, D.E. Armstrong, E. Tarleton, S.G. Roberts, S. Lozano-Perez. How oxidized grain boundaries fail. *Acta Materialia*, 61(2013): 4707-4713.
- [29] L.E. Thomas, S.M. Bruemmer. High-resolution characterization of intergranular attack and stress corrosion cracking of Alloy 600 in high-temperature primary water. *Corrosion*, 56(2000): 572-587.
- [30] G. Bertali, F. Scenini, M. G. Burke. Advanced microstructural characterization of the intergranular oxidation of Alloy 600. *Corrosion Science*, 100 (2015): 474-483.
- [31] M. Meisnar, M. Moody, S. Lozano-Perez. Atom probe tomography of stress corrosion crack tips in SUS316 stainless steels. *Corrosion Science*, 98(2015): 661-671.
- [32] S.M. Bruemmer, M.J. Olszta, M.B. Toloczko, D.K. Schreiber, Grain Boundary Selective Oxidation and Intergranular Stress Corrosion Crack Growth of High-Purity

- Nickel Binary Alloys in High-Temperature Hydrogenated Water. *Corrosion Science*, 131(2018): 310-323.
- [33] D. P. Whittle, Y. Shida, G.C. Wood, F.H. Stott, B.D. Bastow. Enhanced diffusion of oxygen during internal oxidation of nickel-base alloys. *Philosophical Magazine A*, 46(1982): 931-949.
- [34] B. Langelier, S. Y. Persaud, R. C. Newman, G. A. Botton. An atom probe tomography study of internal oxidation processes in Alloy 600. *Acta Materialia*, 109 (2016): 55-68.
- [35] H. K. Birnbaum, P. Sofronis. Hydrogen-enhanced localized plasticity—a mechanism for hydrogen-related fracture. *Materials Science and Engineering: A*, 176(1994): 191-202.
- [36] F. P. Ford. Quantitative prediction of environmentally assisted cracking. *Corrosion*, 52 (1996): 375-395.
- [37] T. Magnin, A. Chambreuil, B. Bayle. The corrosion-enhanced plasticity model for stress corrosion cracking in ductile fcc alloys. *Acta Materialia*, 44(1996): 1457-1470.
- [38] K. Arioka. WR Whitney Award Lecture: Change in bonding strength at grain boundaries before long-term SCC initiation. *Corrosion*, 71(2014): 403-419.
- [39]] B. Langelier, S. Y. Persaud, A. Korinek, T. Casagrande, R. C. Newman, G. A. Botton. Effects of boundary migration and pinning particles on intergranular oxidation revealed by 2D and 3D analytical electron microscopy. *Acta Materialia*, 131 (2017): 280-295.
- [40] Y. Asakura, H. Karasawa, M. Sakagami, S. Uchida. Relationships between corrosion behavior of AISI 304 stainless steel in high-temperature pure water and its oxide film structures. *Corrosion*, 45(1989): 119-124.
- [41] S. Lozano-Perez, T. Yamada, T. Terachi, M. Schröder, C. A. English, G. D. W. Smith, C. R. M. Grovenor, B. L. Eyre. Multi-scale characterization of stress corrosion cracking of cold-worked stainless steels and the influence of Cr content. *Acta Materialia*, 57(2009): 5361-5381.
- [42] G. Bertali, F. Scenini, M. G. Burke. The effect of residual stress on the Preferential Intergranular Oxidation of Alloy 600. *Corrosion Science*: 111 (2016): 494-507.
- [43] Y.S. Lim, H.P. Kim, S.S. Hwang. Microstructural characterization on intergranular stress corrosion cracking of Alloy 600 in PWR primary water environment. *Journal of Nuclear Materials*, 440(2013): 46-54.
- [44] R. W. Staehle. Critical analysis of “tight cracks”. *Corrosion Reviews*, 28 (2010): 1-103.
- [45] K. Arioka, T. Yamada, T. Miyamoto, T. Terachi. Dependence of stress corrosion cracking of alloy 690 on temperature, cold work, and carbide precipitation—role of diffusion of vacancies at crack tips. *Corrosion*, 67(2011): 035006-1.
- [46] J. B. Ferguson, H. F. Lopez. Oxidation products of Inconel alloys 600 and 690 in pressurized water reactor environments and their role in intergranular stress corrosion cracking. *Metallurgical and Materials Transactions A*, 37(2006): 2471-2479.
- [47] G. Pimentel, K. Kruska, O. Calonne, L. Fournier, P. Chou, S. Lozano-Perez. “Advanced High-Resolution Data Mining to Understand Oxide Formation in Austenitic

Alloys”, In Proceedings of the 17th International Conference on Environmental Degradation of Materials in Nuclear Power Systems-Water Reactors, TMS, 2015.

[48] S.M. Bruemmer, B.W. Arey, L.A. Charlot. Influence of chromium depletion on intergranular stress corrosion cracking of 304 stainless steel. *Corrosion*, 48(1992): 42-49.

[49] A. Stratulat, D. E. Armstrong, S. G. Roberts. Micro-mechanical measurement of fracture behaviour of individual grain boundaries in Ni alloy 600 exposed to a pressurized water reactor environment. *Corrosion Science*, 104(2016):9-16.

[50] D. A. Jones. A unified mechanism of stress corrosion and corrosion fatigue cracking. *Metallurgical transactions A*, 16(1985):1133-1141.

[51] B.M. Capell, G. S. Was. Selective internal oxidation as a mechanism for intergranular stress corrosion cracking of Ni-Cr-Fe alloys. *Metallurgical and Materials Transactions A*, 38(2007): 1244-1259.

[52] D. N. Yoon. Chemically induced interface migration in solids. *Annual Review of Materials Science*, 19 (1989): 43-58.

[53] M.F. Ashby. The deformation of plastically non-homogeneous materials. *Philosophical Magazine*, 21(1970): 399-424.

[54] M. Meisnar, A. Vilalta-Clemente, A. Gholinia, M. Moody, A.J. Wilkinson, N. Huin, S. Lozano-Perez. Using transmission Kikuchi diffraction to study intergranular stress corrosion cracking in type 316 stainless steels. *Micron*, 75(2015): 1-10.

[55] S. Lozano-Perez, J. Dohr, M. Meisnar, K. Kruska. SCC in PWRs: learning from a bottom-up approach. *Metallurgical and Materials Transactions E*, 1(2014): 194-210.

[56] F. D. Gioacchino, J. Q. da Fonseca. An experimental study of the polycrystalline plasticity of austenitic stainless steel. *International Journal of Plasticity*, 74(2015): 92-109.

[57] S. A. Attanasio, D. S. Morton, “Measurement of the Ni/NiO transition in Ni-Cr-Fe Alloys and updated data and correlation to quantify the effect of aqueous hydrogen on primary water SCC”, *Proc. 11th Int. Symp. On Environmental Degradation of Materials in Nuclear Power Systems* (Rockville, MD: NRC, 2003).

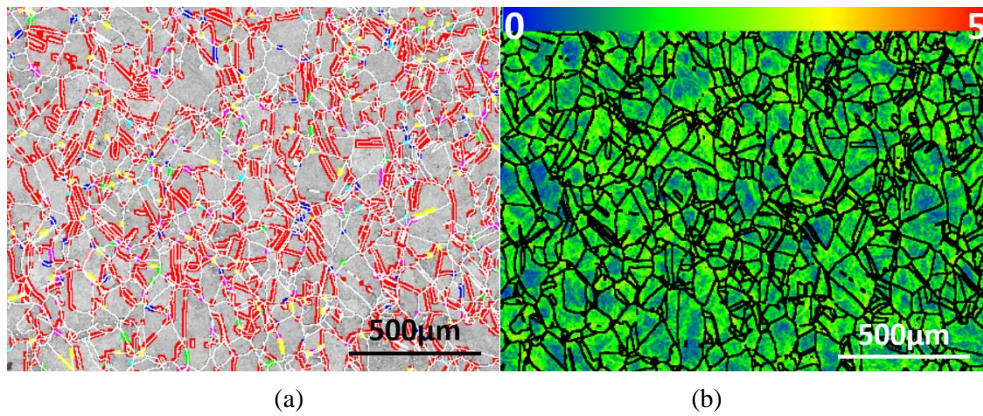


Fig. 1. Microstructure of Alloy 600 obtained from electron backscattered diffraction (step size = 4 μm) analysis. (a) Distribution of grain boundaries (twin boundary in red, random high angle grain boundary in white, coincidence site lattice grain boundaries in yellow, blue, and green); (b) Kernel misorientation map.

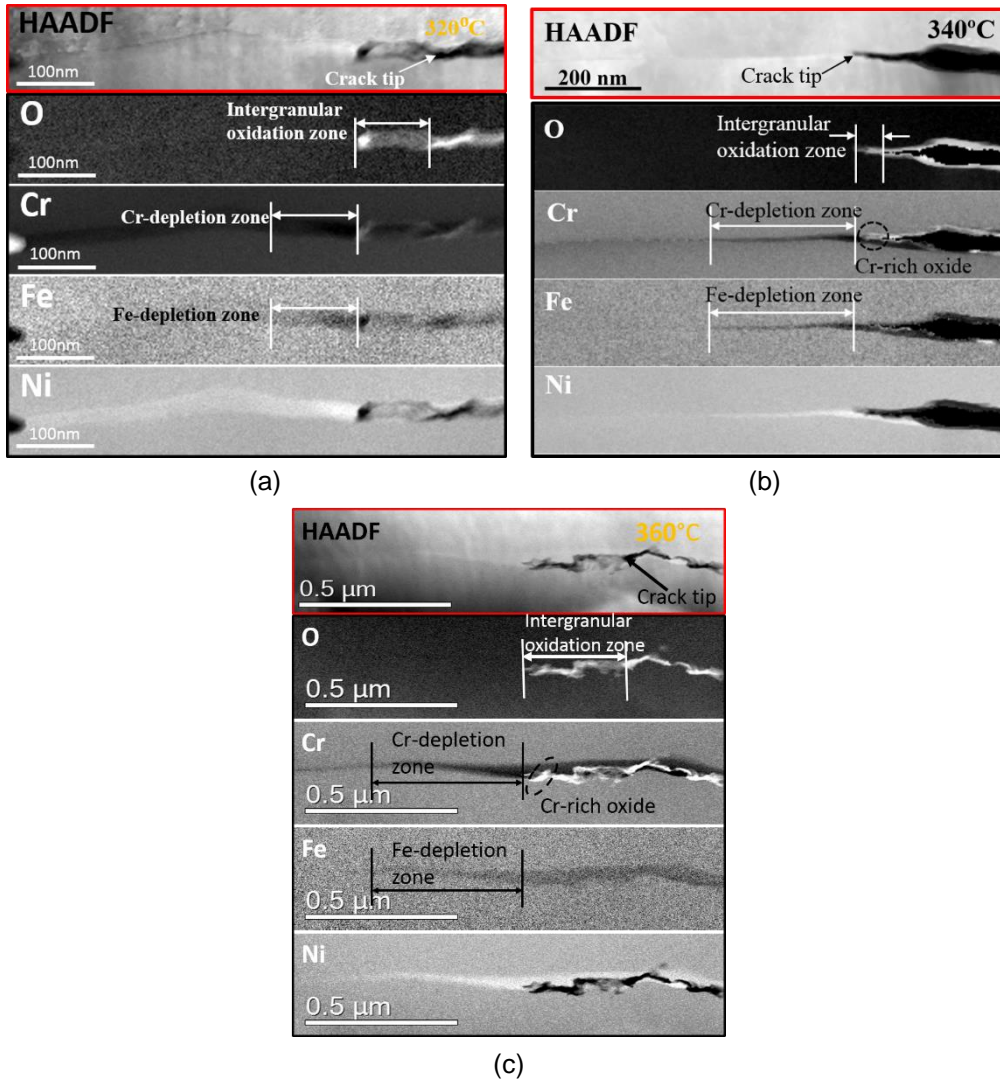
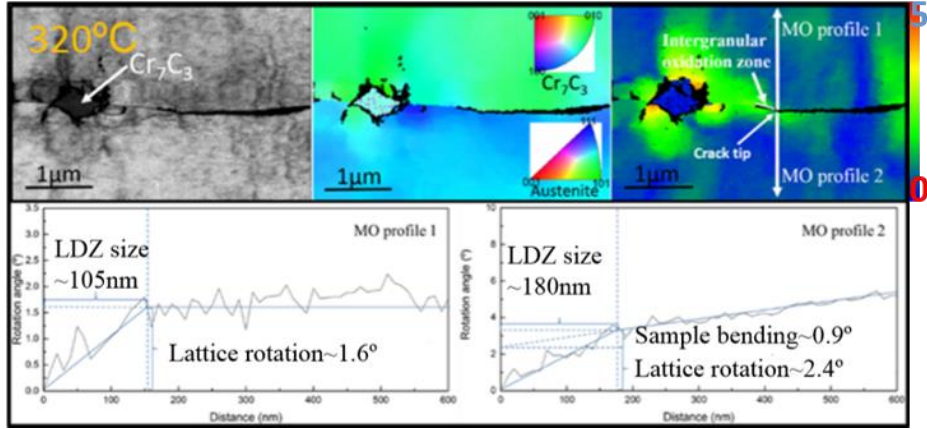
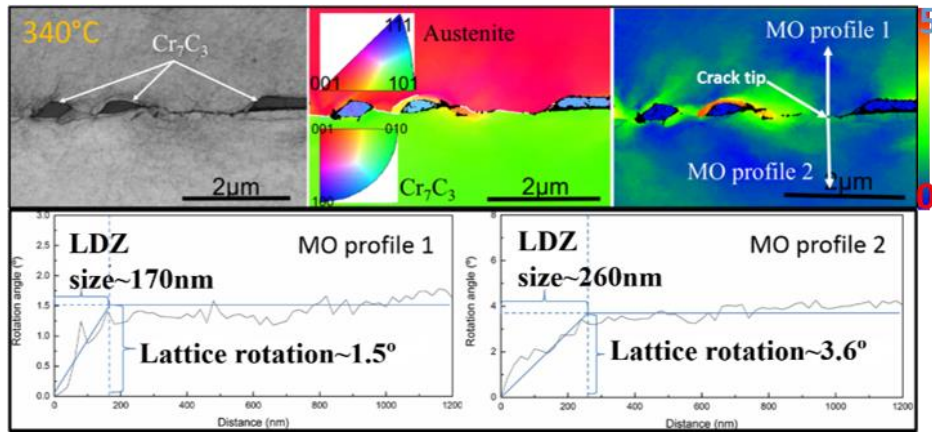


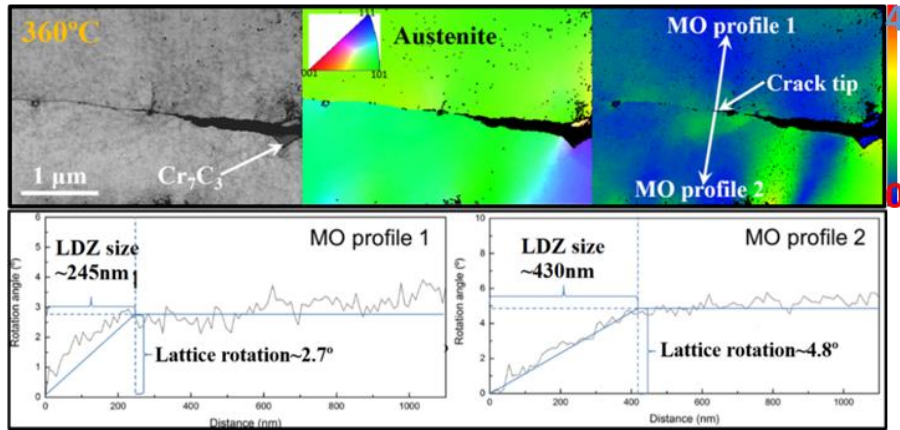
Fig. 2. STEM images and EELS elemental maps showing grain boundary diffusion ahead of the crack tip in high-temperature samples; top: HAADF images, bottom: EELS elemental O K edge and Cr/Fe/Ni L edge maps with step size of 5 nm; Alloy 600 tested at a) 320°C; b) 340°C; c) 360°C.



(a)

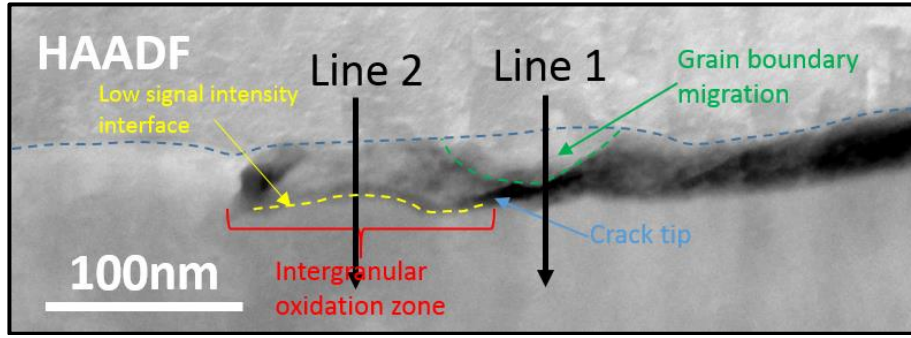


(b)

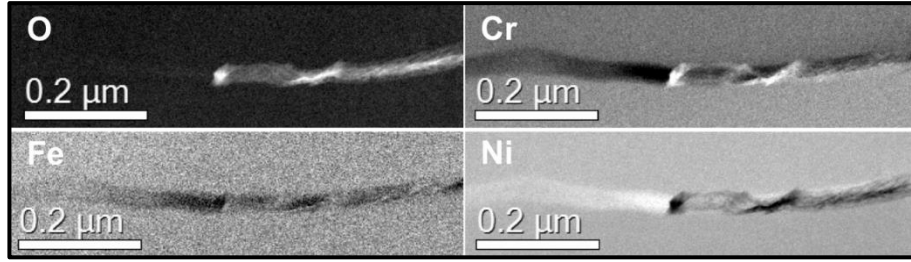


(c)

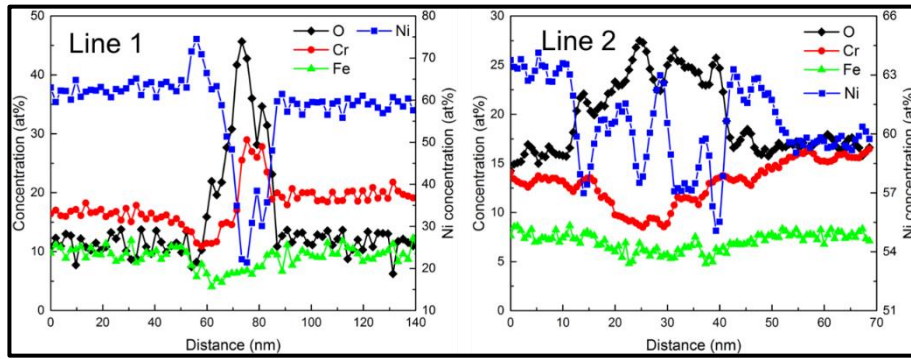
Fig. 3. TKD maps and MO profiles extracted around CTs in high-temperature samples; top: TKD pattern quality map (left), IPFZ map (middle), and average MO map (right); bottom: MO profiles; a) Alloy 600 tested at 320°C, LDZ size~105 nm/lattice rotation $\sim 1.6 \pm 1.1^\circ$ (MO profile 1), LDZ size~180 nm/lattice rotation $\sim 2.4 \pm 1.1^\circ$ (MO profile 2); b) Alloy 600 tested at 340°C, LDZ size~170 nm/lattice rotation $\sim 1.5 \pm 0.9^\circ$ (MO profile 1), LDZ size~260 nm/lattice rotation $\sim 3.6 \pm 0.9^\circ$ (MO profile 2); c) Alloy 600 tested at 360°C, LDZ size~245 nm/lattice rotation $\sim 2.7 \pm 1.1^\circ$ (MO profile 1), LDZ size~430 nm/lattice rotation $\sim 4.8 \pm 1.1^\circ$ (MO profile 2).



(a)



(b)



(c)

(d)

Fig. 4. (a) STEM-HAADF image of a typical crack tip sample tested 320°C with indication of EELS line-scan locations; (b) EELS elemental O K edge and Cr/Fe/Ni L edge maps (step size=1.5 nm); Composition line profiles obtained through EELS analysis performed at the grain boundary migration zone (c); at the IOZ (d).

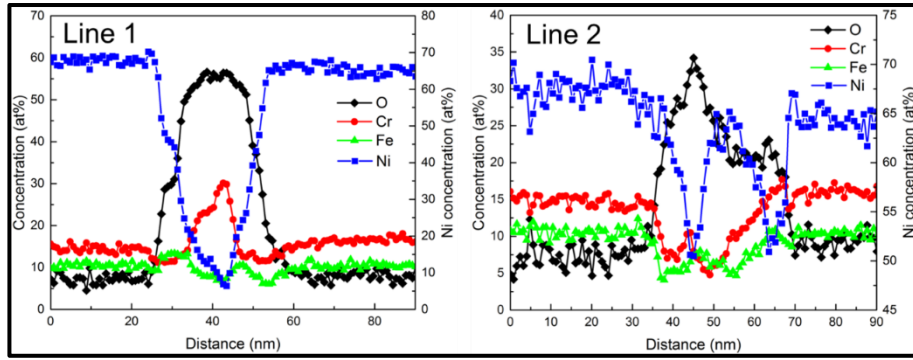
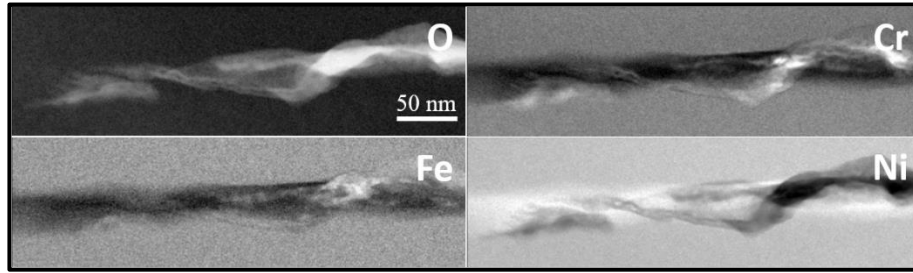
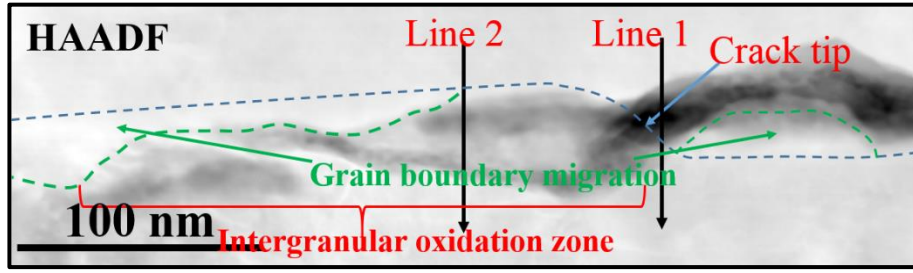
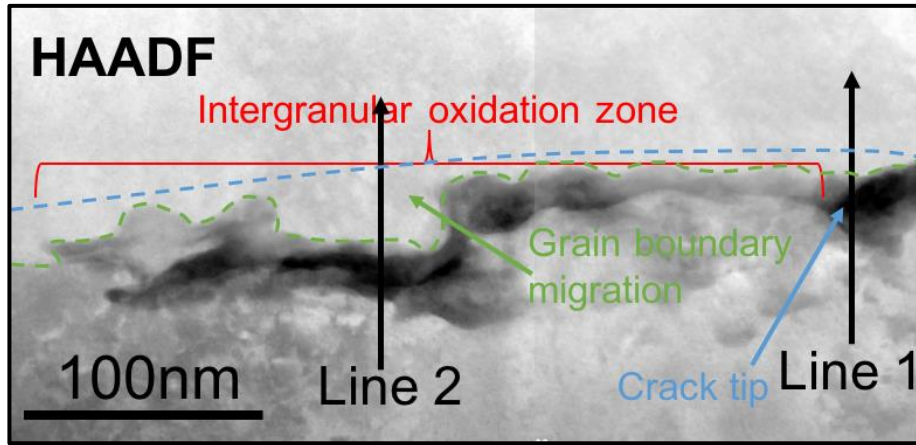
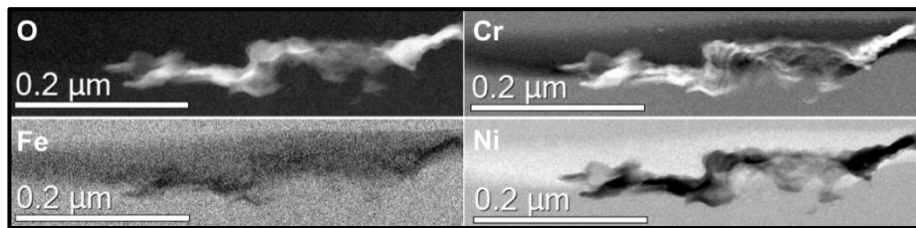


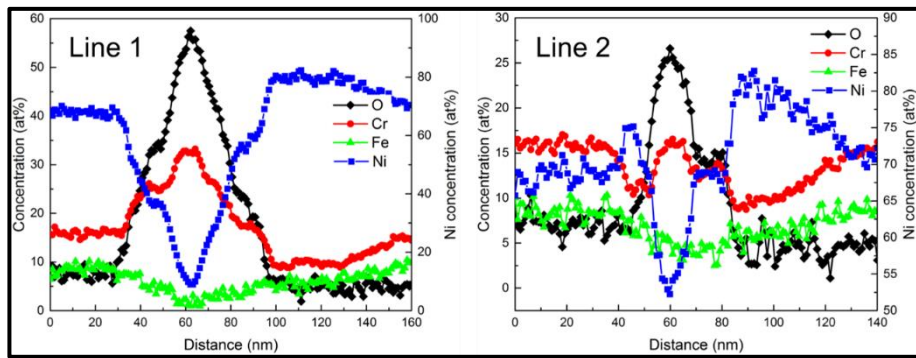
Fig. 5. (a) STEM-HAADF image of a typical crack tip tested at 340°C with indication of EELS line-scan locations; (b) EELS elemental O K edge and Cr/Fe/Ni L edge maps (step size=1.5 nm); Composition line profiles obtained through EELS analysis performed at the crack tip (c); at the IOZ (d).



(a)



(b)



(c)

(d)

Fig. 6. (a) STEM-HAADF image of a typical crack tip sample tested at 360°C with indication of EELS line-scan locations; (b) EELS elemental O K edge and Cr/Fe/Ni L edge maps (step size=1.5 nm); Composition line profiles obtained through EELS analysis performed at the crack tip (c); at the IOZ (d).

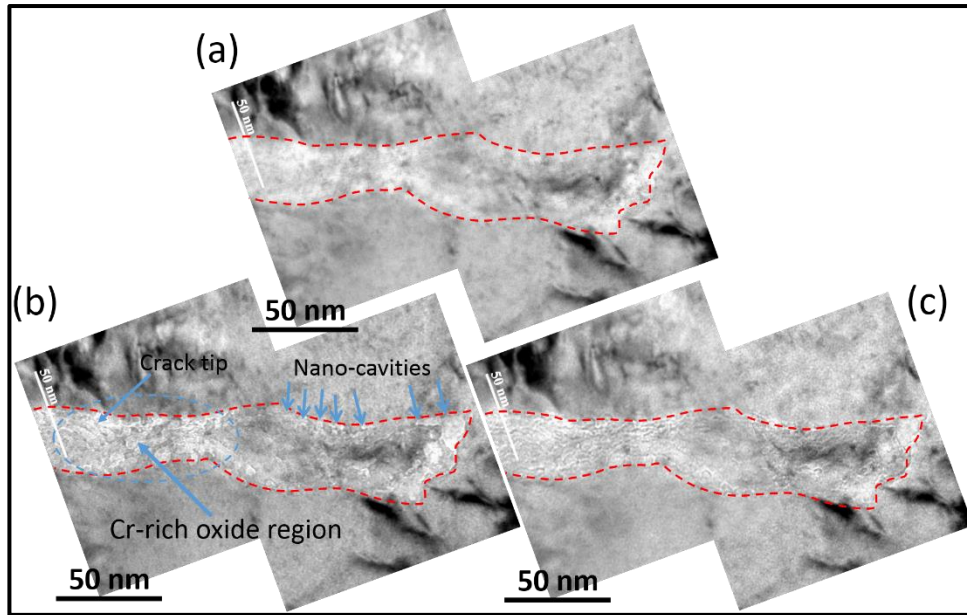


Fig. 7. Fresnel-contrast TEM images taken at (a) focused, (b) underfocused, and (c) overfocused condition to reveal porous structure in a typical crack tip sample tested at 320°C.

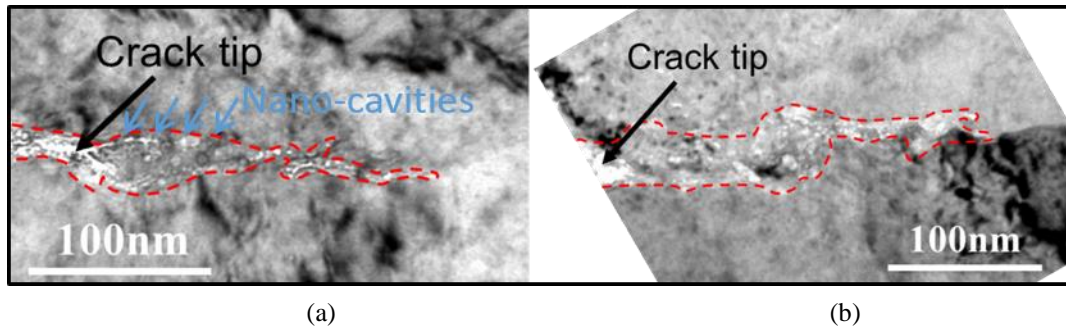


Fig. 8. Fresnel-contrast TEM images taken at underfocused condition to reveal porous structure in the IOZ of typical crack tip samples tested at (a) 340°C and (b) 360°C.

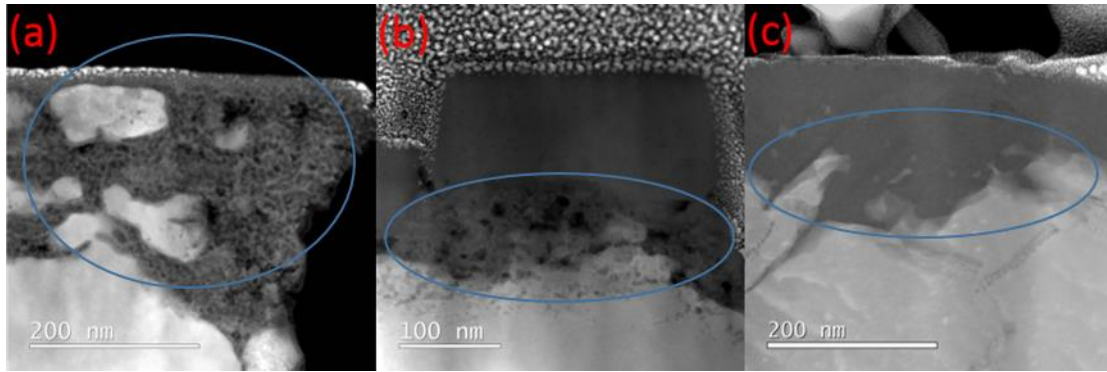


Fig. 9. HAADF images of the surface Cr-rich oxide formed on the surfaces of a) Alloy 600; b) 316SS; c) Alloy 690. Alloy 600 and 316SS were exposed to simulated PWR primary water at 360°C while Alloy 690 was exposed to hydrogenated high temperature steam at 480°C (inner oxide region is circled in the images).

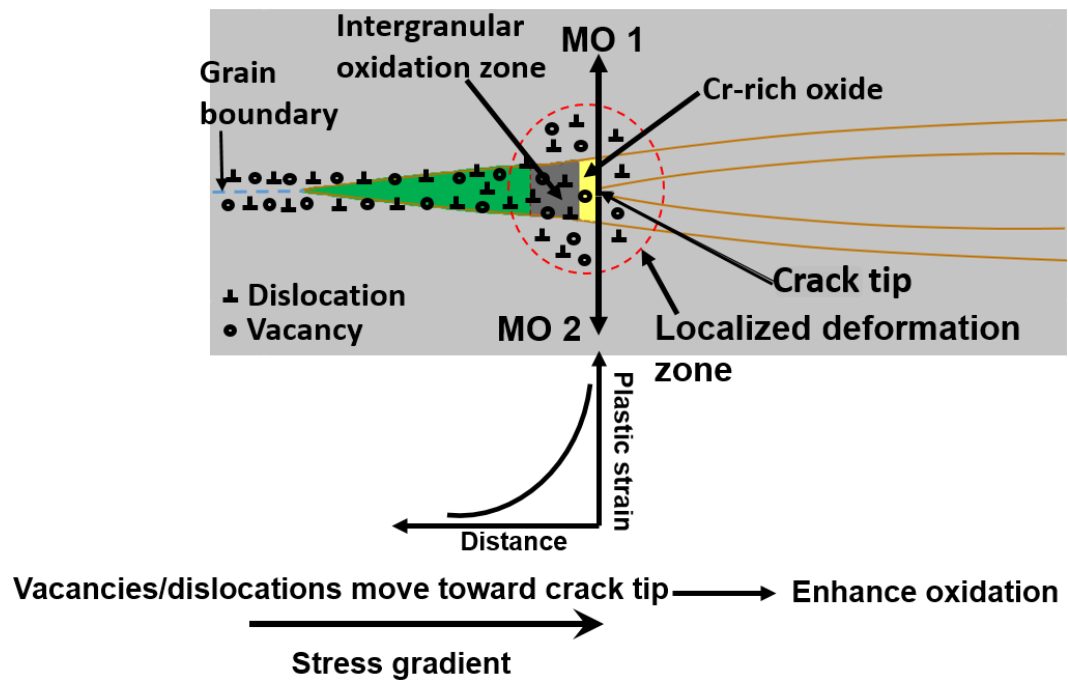


Fig. 10. Schematic illustration of stress gradient-induced defects movement toward high stress areas.

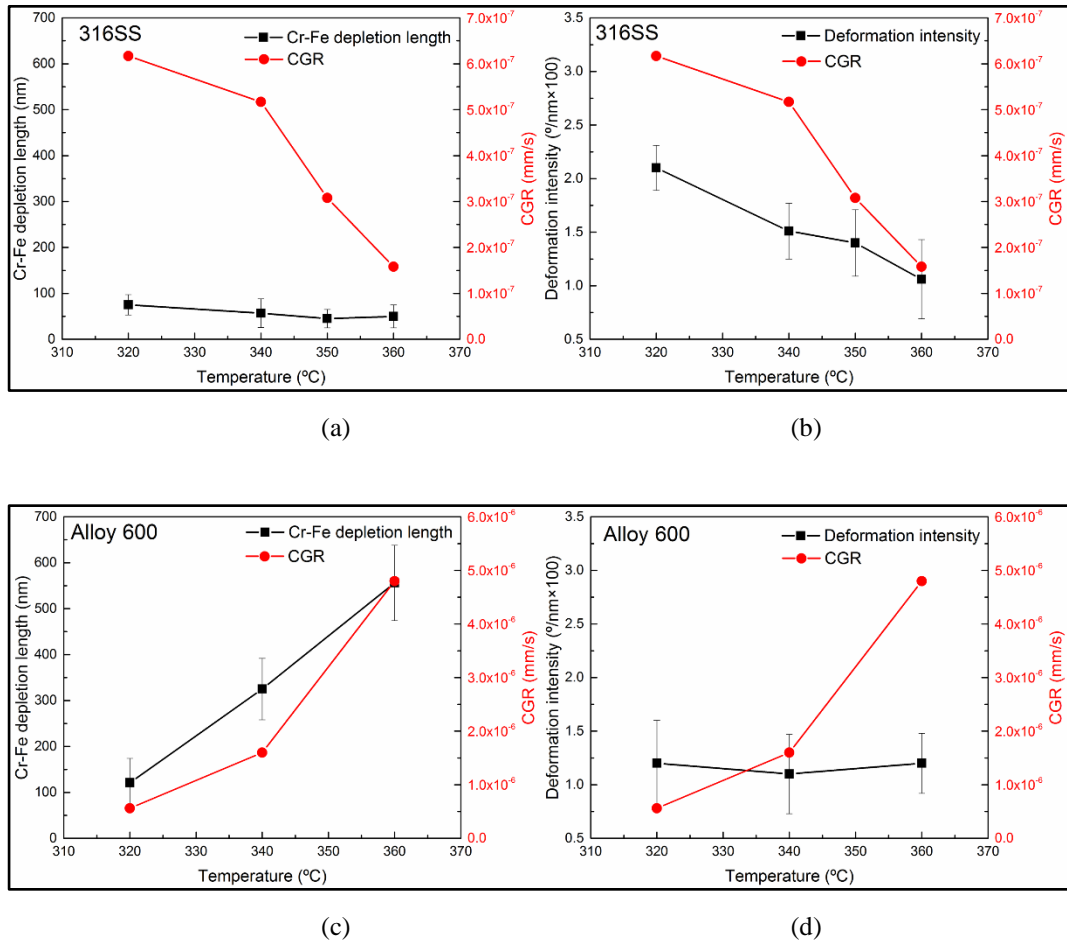


Fig. 11. 316SS: a) illustration of extent of localized deformation around crack tips at different temperatures; b) Illustration of Cr-Fe depletion length ahead of IOZ at different temperatures [19]; Alloy 600: c) illustration of extent of localized deformation around crack tips at different temperatures; d) illustration of Cr-Fe depletion length ahead of IOZ at different temperatures; Red line with circle: temperature dependence of CGR for comparison.